nanomaterials

MDPI

Article

Ultrafast-Laser Micro-Structuring of $LiNi_{0.8}Mn_{0.1}Co_{0.1}O_2$ Cathode for High-Rate Capability of Three-Dimensional Li-ion Batteries

Minh Xuan Tran [1,2], Peter Smyrek [3,4], Jihun Park [5], Wilhelm Pfleging [3,4,*] and Joong Kee Lee [1,2,*]

1 Division of Energy and Environmental Technology, KIST School, Korea University of Science and Technology (UST), Deajeon 34113, Korea
2 Center for Energy Storage Research, Green City Research Institute, Korea Institute of Science and Technology (KIST), Seoul 02792, Korea
3 Karlsruhe Institute of Technology, Institute for Applied Materials, P.O. Box 3640, 76021 Karlsruhe, Germany
4 Karlsruhe Nano Micro Facility, Hermann-von-Helmholtz-Platz 1, 76344 Eggenstein-Leopoldshafen, Germany
5 APC Technology, 108 68 Gangbyeonyeok-ro-4-gil, Gwangjin-gu, Seoul 05116, Korea
* Correspondence: wilhelm.pfleging@kit.edu (W.P.); leejk@kist.re.kr (J.K.L.)

Abstract: Femtosecond ultrafast-laser micro-patterning was employed to prepare a three-dimensional (3D) structure for the tape-casting Ni-rich $LiNi_{0.8}Mn_{0.1}Co_{0.1}O_2$ (NMC811) cathode. The influences of laser structuring on the electrochemical performance of NMC811 were investigated. The 3D-NMC811 cathode retained capacities of 77.8% at 2 C of initial capacity at 0.1 C, which was thrice that of 2D-NMC811 with an initial capacity of 27.8%. Cyclic voltammetry (CV) and impedance spectroscopy demonstrated that the 3D electrode improved the Li^+ ion transportation at the electrode–electrolyte interface, resulting in a higher rate capability. The diffusivity coefficient D_{Li+}, calculated by both CV and electrochemical impedance spectroscopy, revealed that 3D-NMC811 delivered faster Li^+ ion transportation with higher D_{Li+} than that of 2D-NMC811. The laser ablation of the active material also led to a lower charge–transfer resistance, which represented lower polarization and improved Li^+ ion diffusivity.

Keywords: three-dimensional batteries; $LiNi_{0.8}Mn_{0.1}Co_{0.1}O_2$ cathode; femtosecond ultrafast laser; electrode micro-structuring

Citation: Tran, M.X.; Smyrek, P.; Park, J.; Pfleging, W.; Lee, J.K. Ultrafast-Laser Micro-Structuring of $LiNi_{0.8}Mn_{0.1}Co_{0.1}O_2$ Cathode for High-Rate Capability of Three-Dimensional Li-ion Batteries. *Nanomaterials* **2022**, *12*, 3897. https://doi.org/10.3390/nano12213897

Academic Editor: Sergio Brutti

Received: 10 October 2022
Accepted: 2 November 2022
Published: 4 November 2022

1. Introduction

The conventional Li-ion batteries (LIBs) have several limitations, such as low energy density, high cost of the active material, and poor thermal stability [1–3]; hence, their use is limited. However, $LiNi_xMn_yCo_zO_2$ (NMC) has been attracting increasing attention as a promising cathode material with a higher specific capacity and energy density than that of the conventional $LiCoO_2$ (LCO) [4,5]. The Ni-rich NMC cathode, particularly $LiNi_{0.8}Mn_{0.1}Co_{0.8}O_2$ (NMC811), is more cost efficient and has a higher practical specific capacity (200 mAh g^{-1}) than that of the lower-Ni-contained NMC cathode (160 mAh g^{-1}) at an average discharge potential of 3.8 V (vs. Li^+/Li) [6,7]. However, batteries for electric vehicles and applications in smart grid systems require high power to sufficiently charge in a very short time. The output power of LIBs is determined by the transport rate of the Li^+ ion in an electrolyte and active material. Although the NMC cathode materials exhibit superior features in comparison with those of LCO, the NMC cathode is unable to demonstrate the high rate capabilities of conventional electrodes caused by structure disruption and cation-mixing between Li^+ and Ni^{2+} [8–10]. Moreover, the final cell weight and specific cell capacity are functions of the cathode film thickness [11]. Thus, when the thickness of the cathode film increases from 50 µm to 200 µm, the specific cell capacity increases by 29% [12]. Electrodes with thicknesses of 100–200 µm exhibit high energy density, whereas thin electrodes with thicknesses of 10–50 µm exhibit high power density [13,14].

However, the Li^+ diffusion kinetics and mechanical integrity of the film decrease with the electrode film thickness because the active material expands and contracts during continuous charge/discharge processes [15]. Three-dimensional (3D) electrode configuration in LIBs is one of the approaches to overcome the limitations of thick electrode films, such as power losses and mechanical degradation during charge and discharge operations because of high volume expansion [16,17]. Three-dimensional structuring of electrodes improves the electron and ion diffusion kinetics in the electrodes. Moreover, 3D-electrode architectures lead to an increased active surface area, reduced mechanical tensions during electrochemical cycling, and an overall reduced cell impedance [18]. Common methods for 3D configuration in electrodes are the structuring of the substrate or current collector via template deposition of nano-rods or anisotropic etching of silicon. These approaches are only available for thin-film micro batteries and are not feasible for thick-film electrodes [19]. Nonetheless, ultrafast laser structuring is a novel approach to realize the 3D battery concept, and has been applied for thin-film electrodes, including $LiCoO_2$, $Li_2Mn_2O_4$ and SnO_2 [17,20,21]. Moreover, composite electrodes that were patterned with ultrafast lasers have exhibited improved capacities at high charge and discharge currents. The enhancement in the electrochemical performance can also be attributed to the improvement in the wetting of the electrode surface, which results in a decrease in the time and cost required for the vacuum and storage processes during the assembly of LIB cells [12].

In this work, commercial NMC811 was employed as the active material to obtain high energy density. Femtosecond ultrafast laser structuring technology was applied to tape-casted composite electrodes to improve the rate capability of LIBs. In order to investigate the balance of active material loss by ablation from laser structuring and increase in interfacial surface area, ultrafast laser patterning was carried out on NMC811 cathodes with two different thicknesses of 40 and 100 μm. Without structuring, the thin film electrode could deliver better rate capability. When 3D structuring was performed, the rate capability of the thick film electrode was improved to 133 mAh g^{-1} at 5 C. Meanwhile, the structured thin film electrode could not deliver capacity as high as that of post-structuring due to more severe loss of active material. Therefore, the balancing of loss material and increment of interfacial area was a factor that affected improvement in rate capability. The diffusivity of Li^+ ions was studied using cyclic voltammetry (CV) and electrochemical impedance spectroscopy. When laser structuring of the electrode was performed, the transportation of the Li^+ ions improved significantly, with a higher value of D_{Li+}, which could be attributed to the high aspect ratio of 3.7 and increase in surface area of 78%.

2. Materials and Methods

2.1. Material Characterization

The commercial NMC811 powders, with particle size of 10 μm (ECOPro BM, Chungcheongbuk-do, Korea), were used as obtained as the electrode active material. X-ray diffraction (XRD, Rigaku, Tokyo, Japan) analysis was performed using Cu $K\alpha$ radiation (λ = 0.15406 Å) in the 2θ range of 20–80° at a continuous scan mode with a step size of 0.02° and a scan rate of 2° min^{-1}. The morphology and structure of the NMC811 particles were observed using field-emission scanning electron microscopy (FE-SEM, Inspect F50, ThermoFisher, Hillsboro, OR, USA) with an accelerating voltage of 10 kV.

2.2. Ultrafast-Laser Structuring of NMC811 Electrode

The cathode slurry, comprised of NMC811: acetylene black (DB100, Denka, Tokyo, Japan): polyvinylidene fluoride (PVDF, Aldrich, MO, USA), in a weight ratio of 85:10:5, was well mixed in *N*-methylpyrrolidone (NMP, Aldrich, MO, USA) solvent. Then, the slurry was tape-casted on an 18 μm thick aluminum foil as the current collector. After being dried in an oven at 60 °C overnight, a calendaring roll pressure was applied to reduce 10% of the original thickness of the as-prepared cathode to decrease the porosity of the electrodes. The average thickness of the cathodes was 100 μm (exclusive of the Al foil thickness).

Ultrafast-laser-assisted structuring was performed on the calendared electrodes using a fiber laser (Tangerine, Amplitude Systèmes, Pessac, France) operating at a wavelength of λ = 1030 nm with a pulse duration of 380 fs and a laser pulse repetition of 500 kHz. The laser beam was scanned over the sample surface using deflection mirrors with scanning velocities in the range of 100–1500 mm s^{-1}. All experiments were conducted under ambient air and the ablated material was removed by an exhaust.

2.3. Electrochemical Tests

The 2032 coin cell was prepared after the electrodes were dried in a vacuum oven at 80 °C for 12 h. The cathodes were laser cut into discs of 12 mm diameter. A Li metal foil (Wellcos Co., Gyeonggi-do, Korea) disk of Ø18 mm was used as the anode. The cathode and anode in the coin cells were separated by microporous polypropylene (PP) membranes (Celgard 2400, North Carolina, USA) in an electrolyte of 1 M $LiPF_6$ in ethylene carbonate (EC): ethyl methylene carbonate (EMC): diethylene carbonate (DMC) (1:1:1 volume ratio). The cell assembly was performed in a dry room with a dew point temperature of less than −100.2 °C. The electrochemical testing experiments were conducted using a Maccor automated battery tester (MACCOR series-4000, Tulsa, OK, United States) at room temperature of 25 °C. The Li-ion cells were galvanostatically charged/discharged at various currents in the working voltage range of 3.0–4.3 V, after being allowed to rest for 12 h. CV was conducted at scan rates of 0.3–1 mV s^{-1} in the potential range of 3.0–4.3 V. The coin cell was measured by electrochemical impedance spectroscopy (EIS) by applying a frequency range of 1 mHz to 100 kHz to a potentiostat (Bio-Logic Science Instruments, Seyssinet-Pariset, France) with a voltage amplitude of 5 mV.

2.4. Diffusivity Coefficient Calculation

2.4.1. Diffusivity Coefficient by Cyclic Voltammetry

The diffusion coefficient of lithium ion can be determined by the Randles–Sevcik equation:

$$i_P = 0.4463\ \mathrm{mAF}\left(\frac{F}{RT}\right)^{1/2} C_{\mathrm{Li}} D_{\mathrm{Li}}^{1/2} \omega \vartheta^{1/2}, \quad (1)$$

where i_P is peak current (A), m is the mass of active materials-NMC811 (g), A is the effective area of the electrode (cm^2), F is the Faraday constant (96,485 s A mol^{-1}), R is the gas constant (8.314 J K^{-1} mol^{-1}), T is the absolute temperature (K), C is the initial concentration of lithium ion (1.0 mol cm^{-3}), $D_{\mathrm{Li+}}$ is the chemical diffusion coefficient of Li^+ (cm^2 s^{-1}), and ν is the scan rate in mV s^{-1} [22].

2.4.2. Diffusivity Coefficient by EIS

The diffusivity coefficient is calculated using the following equation:

$$D_{\mathrm{Li}^+} = \frac{R^2T^2}{2A^2n^4F^4C^2\sigma^2}, \quad (2)$$

where A (cm^2) is the effective surface area of the electrode, n is the number of exchanged electrons (n = 1), F is Faraday constant, R is gas constant, T is temperature (285 K), C is the initial concentration of Li^+ in electrolyte, and σ is the Warburg factor [23].

The Warburg factor can be determined with the real resistance according to the equation below:

$$Z_{re} = R_s + R_{ct} + \sigma\omega^{1/2}, \quad (3)$$

where R_s (Ω) denotes solution resistance, and ω (Hz) is frequency. The value of σ is extracted from the slope of linear correlation between Z_{re} and $\omega^{-1/2}$.

The effective surface area of electrode (A) used in both Equations (1) and (2) was estimated as the surface area of the electrode. For the 2D-NMC811 electrode, the value of A was calculated as the surface area of the electrode with a diameter of Ø1.2 cm. Effective surface

area of 3D-NMC811 was calculated based on the increasing surface area, as summarized in Table S1.

3. Results and Discussion

The as-received NMC811 particles had a uniform spherical shape with average diameters, D50, of approximately 10 μm, as depicted by the FE–SEM images in Figure S1. The NMC811 spheres were primarily comprised of polyhedral grains of sub-micron size that aggregated to form secondary NMC811 particles, which were consistent with other reports [24,25]. As shown in Figure S1d, the result from the EDX of the selected area suggested that the surface of the NMC811 particles was represented by a composition of a Ni:Mn:Co atomic ratio of 8:1:1, approximately. The crystalline structure of NMC was confirmed by conducting XRD measurements. As illustrated in Figure S2a, the XRD patterns indicated that NMC811 had a layer structure, based on hexagonal α-$NaFeO_2$ with space group R3 m. There were no impurity or secondary phases detected. NMC811 powder had a highly well-defined layer structure, indicated by the appearance of peak splitting of 006/102 and 108/110 (Figure S2b,c) [26,27]. Moreover, the intensity ratio of 003 and 104 peaks, $I_{(003)}/I_{(104)}$, was 1.1, approximately, which indicated a low degree of cation mixing and a good layered structure [7].

The morphologies of the electrodes before and after the structuring by the ultrafast laser are illustrated in Figure 1. After calendaring of the electrodes using a rolling press, the thicknesses of the electrodes were determined as 40 μm and 100 μm, approximately, indicated by the microscopy images in Figure 1. Both electrodes denoted as 2D-NMC811 were used for the laser structuring experiments. The femtosecond laser could remove the composite active materials down to the Al current collector. As depicted in Figure 1a,b, the electrodes were patterned to linear structure with a pitch distance of 200 μm. Figure 1c,d illustrates cross-sectional images of the structured electrodes, denoted as 3D-NMC811. The laser ablated active materials deep to the Al current collector to form a V-shaped channel. The 40 μm-thick NMC811 channel dimensions were determined to be ~25 μm wide and ~38 μm deep, while the 100 μm-thick cathode channels were found to be ~25 μm wide and ~90 μm deep. The edges of the cathode channels were observed to be smooth and uniform.

In order to compare with ablation studies on electrodes with different thicknesses, the aspect ratio *AR* (channel depth divided by channel width of half height), amounts of material loss and interfacial area increments were estimated and listed in Table S1. When the thickness of the electrodes increased from 40 μm to 100 μm, the *AR* value and interfacial area increment increased 4 times, from 0.96 to 3.72, and 20% to 78%, respectively. Along with the *AR* value, loss of active material by ablation from laser structuring decreased from 10% to 6.4% for the 40 μm- and the 100 μm-thick electrodes, respectively. The changes in the above parameters suggested that the laser structuring of electrodes would have more significant effect to improve electrochemical performance of the thick film, 3D-NMC811.

Figure 2a,b exhibits the rate capabilities of 2D- and 3D-NMC811 at various C-rates with thicknesses of 40 and 100 μm, respectively. The 40-μm-thick 2D-NMC811 cathode showed high capacities of 165, 102 and 66 mAh g^{-1} at C-rates of 0.1 C, 1 C and 2 C, respectively. When the thickness of the cathode increased to 100 μm, the capacities at 2 C and 5 C decreased drastically to 48 and 6 mA h g^{-1}, respectively, which was 2 times lower than that of the 40-μm cathode. The deterioration of capacity at high current density in the thick electrode was caused by two aspects: (1) the longer diffusion and migration path of Li^+ ions and (2) the higher local ion-current densities at the electrode/separator interface [28,29]. However, when the ultrafast-laser-structuring was performed, the tendency of rate capability changed remarkably. The 40-μm-thick cathode showed worsened performance with capacity at a high C-rate of 2 C and 5 C decreasing twice to 76 and 31 mAh g^{-1}, respectively, compared to that of 2D-NMC811. On the other hand, the thick 3D-NMC811 electrode (100 μm) showed capacities at 2 C increasing thrice from 48 to 133 mAh g^{-1}, which was higher than that of thin 3D-NMC811 at the same C-rate, as shown in Figure S3. As mentioned above, 3D laser-structuring can drastically improve the electrolyte wetting, and

the active material ablation from laser patterning could provide artificial porosity and an electrolyte reservoir. Thus, laser-induced micro-structuring of the electrode could enhance the electrochemical activation of NMC811 active particles in deeper layers, which resulted in an improvement in the rate capability of thick-film electrodes. Moreover, although interfacial surface area and porosity could increase by means of laser-induced ablation, the negative effect observed for the thin film electrode could be attributed to loss of up to 10% of active material and low *AR* value.

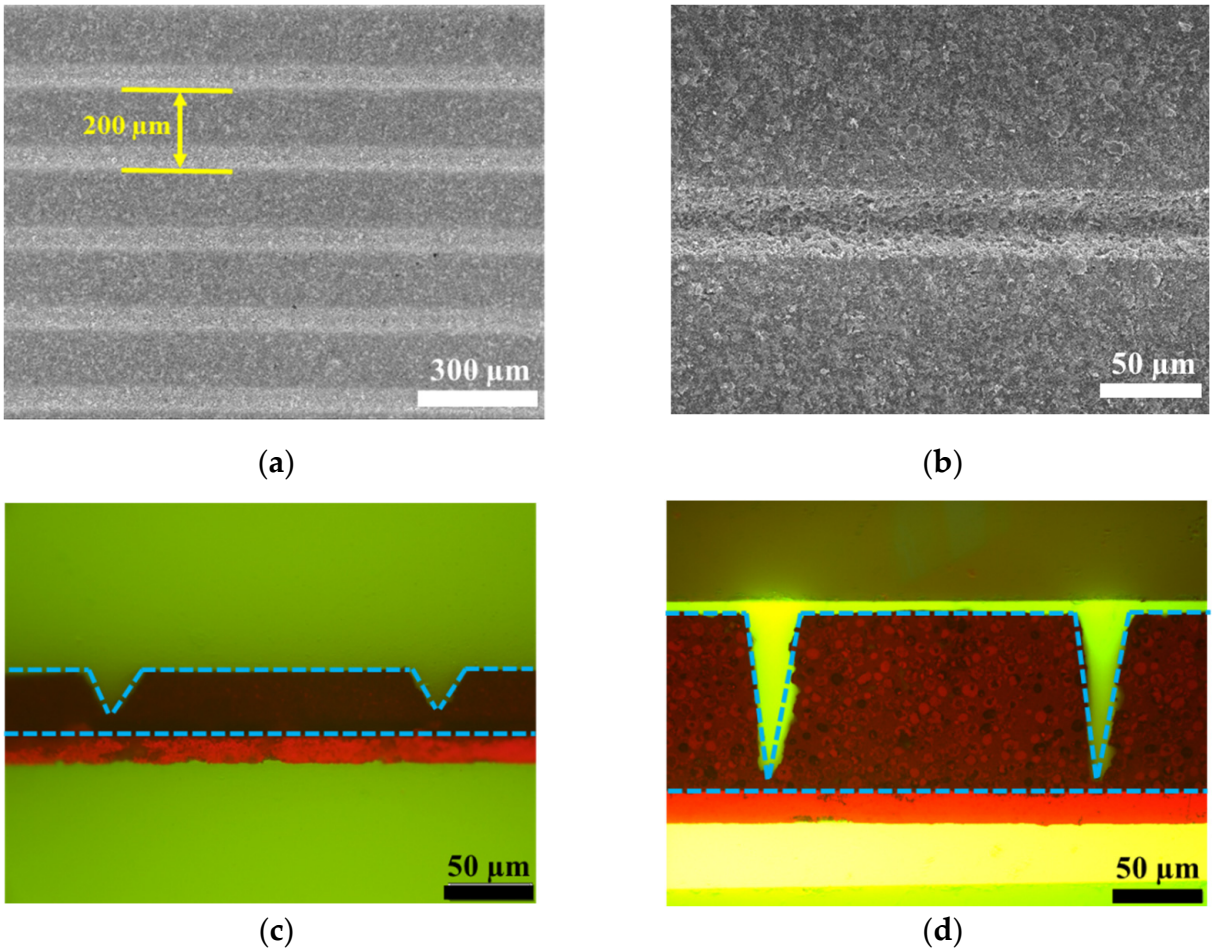

Figure 1. SEM and microscopic images of NMC electrodes (**a**,**b**) top-view of structured electrodes (SEM) at different magnifications, cross section of electrode at (**c**) 40 µm and (**d**) 100 µm (microscope).

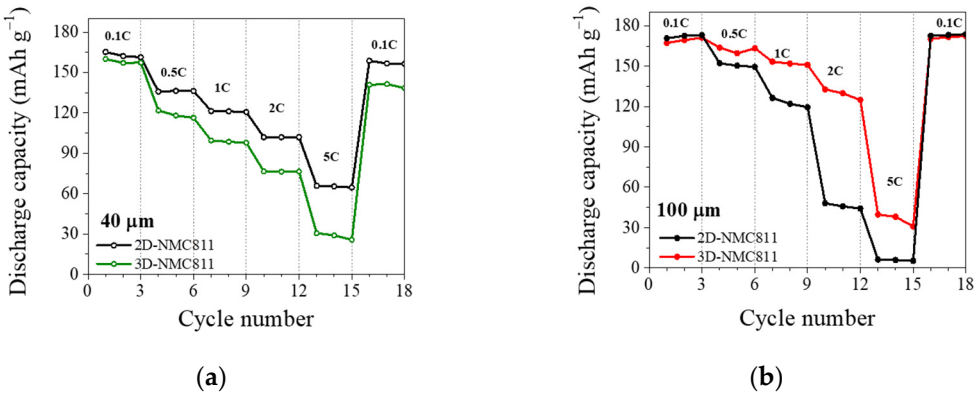

Figure 2. Rate capability performance for unstructured and structured NMC electrodes with thicknesses of (**a**) 40 µm and (**b**) 100 µm.

To study the promotion of Li^+ transportation in the case of a 100-µm-thick structured electrode, CV was performed. The CV curves of NMC811 at a scan rate of 0.3 mV s^{-1} (Figure 3a,b) indicated three distinct anodic/cathodic peaks, which could be assigned to distinct features of the Ni-rich NMC cathode materials. In the positive sweep, the first anodic peaks in the region of 3.4–3.8 V were assigned to the phase transition from a hexagonal to a monoclinic ($H_1 \rightarrow M$) lattice. In the region of potential higher than 3.8 V, there were two anodic peaks at approximately 4.0 and 4.2 V, which were caused by the phase transition from $M \rightarrow H_2$ and $H_2 \rightarrow H_3$, respectively [30,31]. In the first anodic scan, the potential downshifting could be attributed to the initial activation and stabilization of the active material. The current in the first anodic peak did not decrease drastically for the subsequent sweep scan in 3D-NMC811. In contrast, there was a significant change in the intensity of current from the first scan to the following scans in 2D-NMC811. This result indicated a decrease in the interfacial polarization and better reversibility of the 3D-electrode.

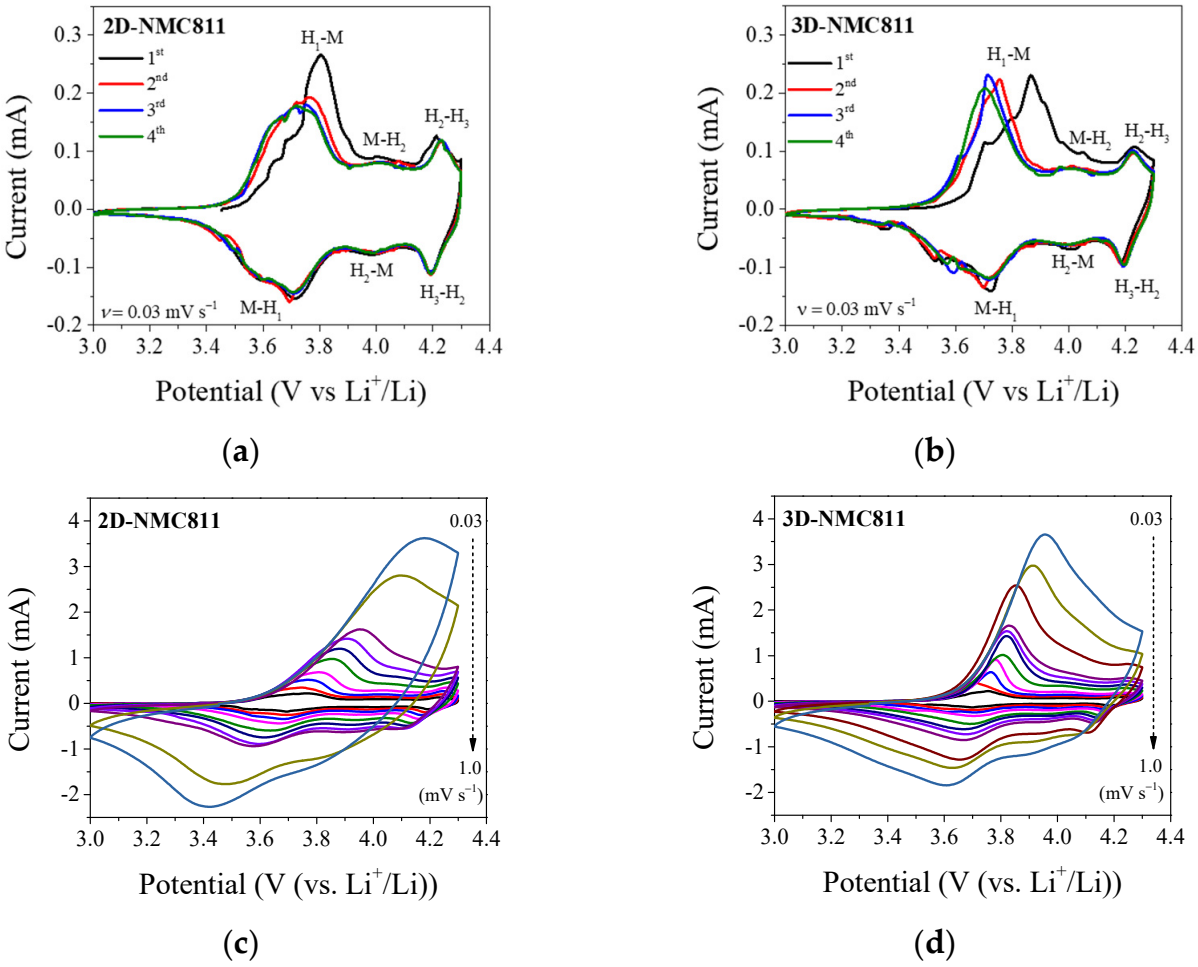

Figure 3. Cyclic voltammetry (CV) data of 2D- and 3D-NMC811 electrodes at (**a**,**b**) 0.3 mV s^{-1} and (**c**,**d**) various scan rates from 0.03 to 1.0 mV s^{-1}.

The potential of the cells with 2D- and 3D-NMC811 were swept at scan rates of 0.03–1.0 mV s^{-1} to calculate the diffusion coefficient (D_{Li+}). As illustrated in Figure 3c,d, the value of the peak currents increased proportionally with the increase in the scan rates, because of the increase in the flux of the charge carrier species at the electrode surface [32]. Since the polarization increased with scan rates, the redox peak positions also shifted to higher and lower voltages for the oxidation (anodic) and the reduction (cathodic) processes, respectively. The redox peak potentials of the structured electrode were significantly higher

than those of the unstructured electrode at the same scan rate. The differences related to the polarization influence were more obvious at a sweep rate higher than 0.5 mV s^{-1}. The mass transfer at the electrode–electrolyte interface was a major factor that caused the polarization in Li-ion cells [33]. The redox peak positions in the CVs upshift and downshift in the charge and discharge processes, respectively, indicated that the enhancement in the mass transfer led to the hindering of the polarization. The 3D-structuring of the electrode by an ultrafast laser could improve the rate performance of NMC811 by enhancement of mass transfer upon electrode. In addition, the diffusion coefficient of the Li^+ ions could be determined by Equation (1) [34]. As depicted in Figure S4, a linear correlation of the peak current density (j) and the square root of scan rate ($\nu^{1/2}$) was obtained. Accordingly, the diffusivity coefficients of 2D-NMC cathode were 16.6 × 10^{-11} and 2.0 × 10^{-11} cm^2 s^{-1} for the oxidation and reduction processes, respectively, as shown in Table S2. When laser patterning was employed, there was an increase in D_{Li+} for the anodic peak to 18.9 × 10^{-11} cm^2 s^{-1}. This result implied that laser structuring of the electrode could improve the Li^+ ion diffusivity in the 3D-NMC811 electrode, due to the increase in the interfacial surface area and improvement in the electrolyte wetting, thereby facilitating fast Li^+ ion transportation.

Moreover, to understand more about the effect of laser structuring on the electrochemical characteristics, impedance analysis was conducted, as illustrated in Figure 4a. The impedance spectroscopy results were consistent with results from CV and diffusivity coefficient. A semicircle in the high frequency range, representing charge transfer resistance (R_{ct}), and a sloping line in the low frequency range, representing Warburg resistance, were observed in both the 2D- and 3D-electrodes. In the Nyquist plots, the semicircle of the 3D-electrode was smaller than that of the 2D electrode. In general, the semicircle in the Nyquist plot represented the impedance values related to the charge–transfer resistance (R_{ct}) obtained by fitting the Nyquist plots, using ZView software, with the corresponding equivalent circuit (Table S2). Moreover, the diffusivity coefficient could also be calculated using σ from Equation (2), which was the Warburg factor extracted from the slope of linear correlation between Z_{re} and $\omega^{-1/2}$, as depicted in Figure S5 [23]. As shown in Figure 4b and Table S2, fresh cells with 3D-NMC811 possessed a lower R_{ct} of 107.7 Ω and a higher D_{Li+} of 3.5 × 10^{-11} cm^2 s^{-1} than those of the 2D-NMC811 electrode (136.6 Ω and 1.6 × 10^{-11} cm^2 s^{-1}). The above results indicated that the 3D-patterning of electrodes could improve Li^+ transportation and decrease electrode polarization [23,35]. The differences in R_{ct} and D_{Li+} values between 2D- and 3D-NMC811 were well-correlated with the data obtained from the CV studies. This result demonstrated that the 3D-structuring of the composite cathode could improve the transportation of Li ions, resulting in enhancement of the rate capability.

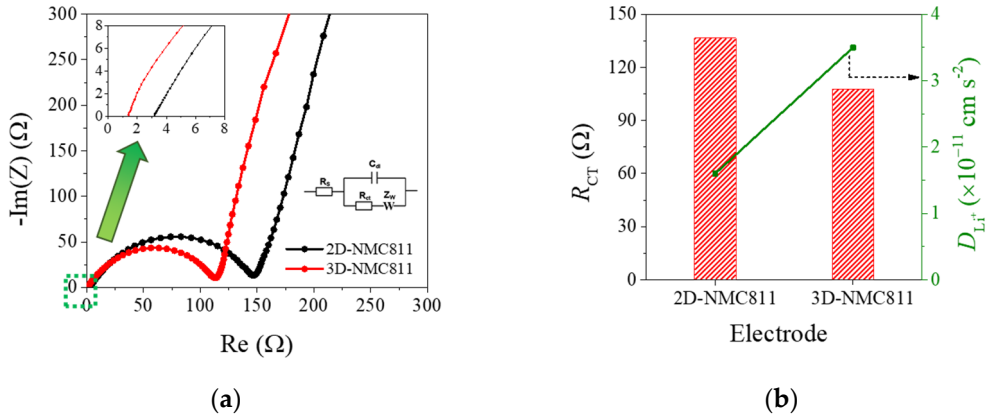

(**a**) (**b**)

Figure 4. (**a**) Nyquist plots of 2D- and 3D-NMC811 electrodes before galvanostatic measurements; (**b**) Fitting results for impedance spectra and calculated D_{Li+} from EIS.

4. Conclusions

Commercially available Ni-rich $LiNi_{0.8}Mn_{0.1}Co_{0.1}O_2$ (NMC811), with a high capacity and energy density, was used as the cathode material for a Li ion battery. The tape-casted composite electrodes were micro-structurally modified by a femtosecond ultrafast laser to generate 3D-electrode configuration. The 3D-patterning of electrodes with different thicknesses resulted in different aspect ratio values and material losses. Higher aspect ratio and increment of interfacial surface area, and lower active material loss were observed in the thick-film 3D-NMC811. The laser structuring improved the capacity of the thick film cathode at a high rate but failed to have a positive effect on that of the thin film electrode. The 3D-modification of the cathode improved the mass transfer of Li^+ ions into the deep layers of the electrode, as well as the wetting capability of the electrolyte. The diffusivity coefficient of the Li^+ ions, determined by CV and EIS, demonstrated that the 3D-NMC811 possessed a lower value of D_{Li+} than that of 2D-NMC811. The charge transfer resistance was lower, which indicated a lower polarization and improved Li^+ ion diffusivity. Faster ion transportation in 3D-NMC811 resulted in a higher rate capability of 133 mAh g^{-1} at a C-rate of 2 C, which was 77.8% of the initial capacity at 0.1 C and thrice that of 2D-NMC811. Laser structuring to realize the 3D-battery concept could be an approach to commercialize high-energy NMC811 cathode materials with high power output.

Supplementary Materials: The following supporting information can be downloaded at: https://www.mdpi.com/article/10.3390/nano12213897/s1, Figure S1: Morphology of NMC811 particles; Figure S2: XRD patterns of NMC particles; Figure S3: Galvanostatic charge/ discharge profiles; Figure S4: Diffusivity coefficient calculation; Figure S5: Linear fit lines demonstrating correlation between Z_{re} and $\omega^{-1/2}$; Table S1: Summary of effect of laser structuring on electrodes at various thicknesses; Table S2: Fitting results for impedance spectra and calculated D_{Li+} from CVs and electrochemical impedance spectroscopy.

Author Contributions: Conceptualization, M.X.T. and J.K.L.; methodology, P.S.; software, P.S.; validation, M.X.T. and P.S.; formal analysis, M.X.T.; investigation, P.S.; resources, J.K.L. and W.P.; data curation, M.X.T.; writing—original draft preparation, M.X.T.; writing—review and editing, J.K.L. and W.P.; visualization, M.X.T.; supervision, J.K.L.; project administration, J.K.L., J.P. and W.P.; funding acquisition, J.K.L. and W.P. All authors have read and agreed to the published version of the manuscript.

Funding: This project received funding from the German Research Foundation (DFG, project No. 392322200).

Data Availability Statement: Not applicable.

Acknowledgments: This study was supported by the KIST Institutional Program (2E31863, 2V09284). We are grateful to Jan Rakebrandt for technical assistance in laser processing. In addition, the support for laser materials processing by the Karlsruhe Nano Micro Facility (KNMF, http://www.knmf.kit.edu/), a Helmholtz research infrastructure at KIT, is gratefully acknowledged.

Conflicts of Interest: The authors declare no conflict of interest.

References

1. Yang, Y.; Okonkwo, E.G.; Huang, G.; Xu, S.; Sun, W.; He, Y. On the sustainability of lithium ion battery industry—A review and perspective. *Energy Storage Mater.* **2021**, *36*, 186–212. [CrossRef]
2. Liu, J.; Long, J.; Du, S.; Sun, B.; Zhu, S.; Li, J. Three-Dimensionally Porous Li-Ion and Li-S Battery Cathodes: A Mini Review for Preparation Methods and Energy-Storage Performance. *Nanomaterials* **2019**, *9*, 441. [CrossRef]
3. Hu, X.; Xu, L.; Lin, X.; Pecht, M. Battery Lifetime Prognostics. *Joule* **2020**, *4*, 310–346. [CrossRef]
4. Pimlott, J.L.; Street, R.J.; Down, M.P.; Banks, C.E. Electrochemical Overview: A Summary of $ACo_xMn_yNi_zO_2$ and Metal Oxides as Versatile Cathode Materials for Metal-Ion Batteries. *Adv. Func. Mater.* **2021**, *31*, 2107761. [CrossRef]
5. Xu, C.; Reeves, P.J.; Jacquet, Q.; Grey, C.P. Phase Behavior during Electrochemical Cycling of Ni-Rich Cathode Materials for Li-Ion Batteries. *Adv. Energy Mater.* **2021**, *11*, 2003404. [CrossRef]
6. You, B.; Wang, Z.; Shen, F.; Chang, Y.; Peng, W.; Li, X.; Guo, H.; Hu, Q.; Deng, C.; Yang, S.; et al. Research Progress of Single-Crystal Nickel-Rich Cathode Materials for Lithium Ion Batteries. *Small Methods* **2021**, *5*, 2100234. [CrossRef] [PubMed]

7. Li, L.; Wang, D.; Xu, G.; Zhou, Q.; Ma, J.; Zhang, J.; Du, A.; Cui, Z.; Zhou, X.; Cui, G. Recent progress on electrolyte functional additives for protection of nickel-rich layered oxide cathode materials. *J. Energy Chem.* **2022**, *65*, 280–292. [CrossRef]
8. Zhang, H.; He, X.; Chen, Z.; Yang, Y.; Xu, H.; Wang, L.; He, X. Single-Crystalline Ni-Rich $LiNi_xMn_yCo_{1-x-y}O_2$ Cathode Materials: A Perspective. *Adv. Energy Mater.* **2022**, 2202022. [CrossRef]
9. Li, X.; Gao, A.; Tang, Z.; Meng, F.; Shang, T.; Guo, S.; Ding, J.; Luo, Y.; Xiao, D.; Wang, X.; et al. Robust Surface Reconstruction Induced by Subsurface Ni/Li Antisites in Ni-Rich Cathodes. *Adv. Funct. Mater.* **2021**, *31*, 2010291. [CrossRef]
10. Xia, Y.; Zheng, J.; Wang, C.; Gu, M. Designing principle for Ni-rich cathode materials with high energy density for practical applications. *Nano Energy* **2018**, *49*, 434–452. [CrossRef]
11. Wood, D.L.; Li, J.; Daniel, C. Prospects for reducing the processing cost of lithium ion batteries. *J. Power Sources* **2015**, *275*, 234–242. [CrossRef]
12. Pfleging, W. A review of laser electrode processing for development and manufacturing of lithium-ion batteries. *Nanophotonics* **2018**, *7*, 549–573. [CrossRef]
13. Johnson, B.A.; White, R.E. Characterization of commercially available lithium-ion batteries. *J. Power Sources* **1998**, *70*, 48–54. [CrossRef]
14. Kim, U.S.; Shin, C.B.; Kim, C.-S. Modeling for the scale-up of a lithium-ion polymer battery. *J. Power Sources* **2009**, *189*, 841–846. [CrossRef]
15. Du, Z.; Wood, D.L.; Daniel, C.; Kalnaus, S.; Li, J. Understanding limiting factors in thick electrode performance as applied to high energy density Li-ion batteries. *J. Appl. Electrochem.* **2017**, *47*, 405–415. [CrossRef]
16. Pfleging, W.; Pröll, J. A new approach for rapid electrolyte wetting in tape cast electrodes for lithium-ion batteries. *J. Mater. Chem. A* **2014**, *2*, 14918–14926. [CrossRef]
17. Hudaya, C.; Halim, M.; Pröll, J.; Besser, H.; Choi, W.; Pfleging, W.; Seifert, H.J.; Lee, J.K. A polymerized C_{60} coating enhancing interfacial stability at three-dimensional $LiCoO_2$ in high-potential regime. *J. Power Sources* **2015**, *298*, 1–7. [CrossRef]
18. Baggetto, L.; Niessen, R.A.H.; Roozeboom, F.; Notten, P.H.L. High Energy Density All-Solid-State Batteries: A Challenging Concept Towards 3D Integration. *Adv. Funct. Mater.* **2008**, *18*, 1057–1066. [CrossRef]
19. Lim, D.G.; Chung, D.-W.; Kohler, R.; Proell, J.; Scherr, C.; Pfleging, W.; García, R.E. Designing 3D Conical-Shaped Lithium-Ion Microelectrodes. *J. Electrochem. Soc.* **2014**, *161*, A302–A307. [CrossRef]
20. Pröll, J.; Kohler, R.; Torge, M.; Bruns, M.; Przybylski, M.; Ulrich, S.; Seifert, H.J.; Pfleging, W. Laser-adjusted three-dimensional Li-Mn-O cathode architectures for secondary lithium-ion cells. In Proceedings of the SPIE LASE, San Francisco, CA, USA, 17 February 2012; pp. 1–10.
21. Park, J.H.; Kohler, R.; Pfleging, W.; Choi, W.; Seifert, H.J.; Lee, J.K. Electrochemical behavior of a laser microstructured fluorine doped tin oxide anode layer with a plasma pretreatment for 3D battery systems. *RSC Adv.* **2014**, *4*, 4247–4252. [CrossRef]
22. Xuan Tran, M.; Woo, J.-Y.; Nguyen, T.-A.; Lee, S.-W.; Kee Lee, J. Thermolytically grafted silicon particles with ultrathin carbonaceous coating rich of phenyl moieties as lithium-storage anode material. *Chem. Engin. J.* **2020**, *395*, 125169. [CrossRef]
23. Huang, Y.; Jin, F.-M.; Chen, F.-J.; Chen, L. Improved cycle stability and high-rate capability of Li_3VO_4-coated $Li[Ni_{0.5}Co_{0.2}Mn_{0.3}]O_2$ cathode material under different voltages. *J. Power Sources* **2014**, *256*, 1–7. [CrossRef]
24. Li, J.; Downie, L.E.; Ma, L.; Qiu, W.; Dahn, J.R. Study of the Failure Mechanisms of $LiNi_{0.8}Mn_{0.1}Co_{0.1}O_2$ Cathode Material for Lithium Ion Batteries. *J. Electrochem. Soc.* **2015**, *162*, A1401–A1408. [CrossRef]
25. Kim, H.; Kim, M.G.; Jeong, H.Y.; Nam, H.; Cho, J. A new coating method for alleviating surface degradation of $LiNi_{0.6}Co_{0.2}Mn_{0.2}O_2$ cathode material: Nanoscale surface treatment of primary particles. *Nano Lett.* **2015**, *15*, 2111–2119. [CrossRef] [PubMed]
26. Yang, K.; Fan, L.-Z.; Guo, J.; Qu, X. Significant improvement of electrochemical properties of AlF_3-coated $LiNi_{0.5}Co_{0.2}Mn_{0.3}O_2$ cathode materials. *Electrochim. Acta* **2012**, *63*, 363–368. [CrossRef]
27. Bie, X.; Du, F.; Wang, Y.; Zhu, K.; Ehrenberg, H.; Nikolowski, K.; Wang, C.; Chen, G.; Wei, Y. Relationships between the crystal/interfacial properties and electrochemical performance of $LiNi_{0.33}Co_{0.33}Mn_{0.33}O_2$ in the voltage window of 2.5–4.6V. *Electrochim. Acta* **2013**, *97*, 357–363. [CrossRef]
28. Singh, M.; Kaiser, J.; Hahn, H. Thick Electrodes for High Energy Lithium Ion Batteries. *J. Electrochem. Soc.* **2015**, *162*, A1196–A1201. [CrossRef]
29. Wang, J.S.; Liu, P.; Sherman, E.; Verbrugge, M.; Tataria, H. Formulation and characterization of ultra-thick electrodes for high energy lithium-ion batteries employing tailored metal foams. *J. Power Sources* **2011**, *196*, 8714–8718. [CrossRef]
30. Jung, R.; Metzger, M.; Maglia, F.; Stinner, C.; Gasteiger, H.A. Oxygen Release and Its Effect on the Cycling Stability of $LiNi_xMn_yCo_zO_2$ (NMC) Cathode Materials for Li-Ion Batteries. *J. Electrochem. Soc.* **2017**, *164*, A1361–A1377. [CrossRef]
31. Yang, J.; Xia, Y. Suppressing the Phase Transition of the Layered Ni-Rich Oxide Cathode during High-Voltage Cycling by Introducing Low-Content Li_2MnO_3. *ACS Appl. Mater. Interfaces* **2016**, *8*, 1297–1308. [CrossRef]
32. Laskar, M.R.; Jackson, D.H.; Xu, S.; Hamers, R.J.; Morgan, D.; Kuech, T.F. Atomic Layer Deposited MgO: A Lower Overpotential Coating for $Li[Ni_{0.5}Mn_{0.3}Co_{0.2}]O_2$ Cathode. *ACS Appl. Mater. Interfaces* **2017**, *9*, 11231–11239. [CrossRef] [PubMed]
33. Liu, X.; Li, H.; Li, D.; Ishida, M.; Zhou, H. PEDOT modified $LiNi_{1/3}Co_{1/3}Mn_{1/3}O_2$ with enhanced electrochemical performance for lithium ion batteries. *J. Power Sources* **2013**, *243*, 374–380. [CrossRef]

34. Bard, A.J.; Faulkner, L.R. *Electrochemical Methods: Fundamentals and Applications*; Wiley: New York, NY, USA, 2000.
35. Bai, Y.; Wang, X.; Yang, S.; Zhang, X.; Yang, X.; Shu, H.; Wu, Q. The effects of $FePO_4$-coating on high-voltage cycling stability and rate capability of $Li[Ni_{0.5}Co_{0.2}Mn_{0.3}]O_2$. *J. Alloys Compd.* **2012**, *541*, 125–131. [CrossRef]